Modelling forward vortex flow in a microwave plasma

Chemical Engineering Journal 503 (2025) 158072

Contents lists available at ScienceDirect

Chemical Engineering Journal

journal homepage: www.elsevier.com/locate/cej

Modelling forward vortex flow in a microwave plasma

P.W.C. Groen [a,*], W.A. Bongers [a], J.F.J. Janssen [c], T.W.H. Righart [d], A.W. van de Steeg [a], A.J. Wolf [a], M.C.M. van de Sanden [a,b,e], F.J.J. Peeters [a,f]

[a] DIFFER - Dutch Institute For Fundamental Energy Research, De Zaale 20, 5612 AJ, Eindhoven, The Netherlands
[b] Department of Applied Physics, Eindhoven University of Technology, PO Box 513, 5600 MB Eindhoven, The Netherlands
[c] Plasma Matters, De Zaale, 19, 5612 AJ Eindhoven, The Netherlands
[d] Department of Circular Chemical Engineering, Faculty of Science and Engineering, Maastricht University, PO Box 616, 6200 MD Maastricht, The Netherlands
[e] Eindhoven Institute for Renewable Energy Systems, Eindhoven University of Technology, P.O. Box 513, 5600 MB Eindhoven, The Netherlands
[f] LeydenJar, Luchthavenweg 10, 5657 EB Eindhoven, The Netherlands

ARTICLE INFO

Keywords:
CO_2 plasma
Microwave plasma
Reactor modelling
Fluid modelling
Vortex

ABSTRACT

In this paper, 3D, turbulent fluid models of a CO_2, forward vortex, microwave plasma are presented. The high temperature (3000–7000 K), heterogeneous plasma is modelled as a turbulent heated gas. In the turbulence (RANS) models the heat source is based on experimental observations, and the gas is described as a single species representing the plasma mixture. The model is validated using experimentally measured temperature values from literature, and works well for the investigated pressures, except for downstream values and the maximum temperature for 100 mbar. Agreement of the model with experiment is best in the plasma region, and depends on the shape of the heat source and the choice of turbulent Prandtl number. It is shown that the preferential model is the k–ω RANS model. We conclude that the k–ω model with a gas composition represented by a single species can provide sufficiently accurate temperature profiles for in silico engineering of high temperature CO_2 plasma reactors.

1. Introduction

Plasmas are investigated for efficient dissociation of CO_2 into CO and O_2 [1–3]. One of the concepts in the plasma reactors used is the vortex (swirling) flow, e.g. in gliding arcs [4,5] or in microwave plasmas [2,6–8]. Multiple configurations of a microwave plasma reactor can be utilised, e.g. using a forward (also called 'direct') vortex flow, or a reverse (or 'counter') vortex flow [2]. The vortex is used to promote a rotationally symmetric gas temperature profile which provides its stability, and to concentrate cold injected gas near the quartz tube, thus protecting it from heating damage, without the need of a coolant. In a forward vortex configuration the exhaust is placed downstream.

Vortex flow has been studied extensively, both experimentally and numerically [9–11]. Numerous different setups and configurations are possible, for instance the number and position of the (tangential) inlets or vanes, or the position of the exhaust. Also the addition of quenching nozzles has been investigated, e.g. a De Laval nozzle [12], as well as other types of nozzle [13] to improve conversion and energy efficiency.

A well known phenomenon of vortex flow, is the formation of a recirculation cell [6,14,15], i.e. a zone of reverse (return) flow, that is terminated at some position on the axis, the stagnation point, i.e. where the convective axial velocity is zero, see Fig. 1. This recirculation zone is then enveloped by a forward swirling outer flow. Also multiple recirculation cells have been observed (in a reverse vortex tube [6,16] and their Ref. [17]).

The vortex flow has an impact on the performance of the reactor. It is most efficient when recombination of CO and O is suppressed. Therefore, ideally, the outer, forward swirling flow would carry these dissociation products to the exhaust, and CO_2 would, through recirculation, re-enter the heated zone to be dissociated. Moreover, the CO and O then also would need to cool down fast enough (quenching) and O should preferentially react with incoming CO_2 to form additional CO and O_2 [14,18,19]. Whether such a scenario could happen also depends on the temperature distribution, which results from an interplay of chemistry and flow.

To gain more insight in the influence of the flow on plasma properties, Computational Fluid Dynamics (CFD) modelling is essential to be able to engineer an optimal CO_2 microwave reactor. Having a turbulent swirling flow present that is not axially symmetric, because of the helical nature, leads to the need of a three dimensional turbulent model.

The role of turbulent transport on plasma processing has been investigated [14], but the influence of the fluid flow (both turbulent

* Corresponding author.
E-mail address: p.w.c.groen@differ.nl (P.W.C. Groen).

https://doi.org/10.1016/j.cej.2024.158072
Received 9 February 2024; Received in revised form 26 October 2024; Accepted 25 November 2024
Available online 30 November 2024

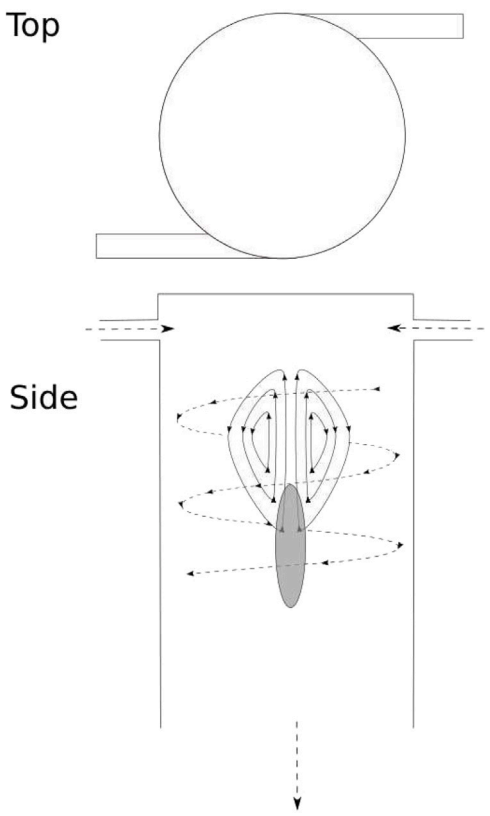

Fig. 1. Schematic impression of a tube with a forward vortex flow; top and side (cut) view. The top of the tube is closed. Two (tangential) inlet tubes are situated somewhat down the top. In the centre a recirculation cell is shown, with backflow at its centre and downward flow at the sides, resulting in no net mass flow from the cell. Outside of the cell a swirling, net forward, flow is shown (dashed line). The plasma is drawn in grey, schematically, at an arbitrary relative axial position to the recirculation cell. The azimuthal component of the recirculation flow is ignored in this impression for clarity.

and swirling) on the plasma (transport) properties is still not fully understood. Furthermore, vortex flow in combination with a hot plasma has not yet been studied thoroughly. Studies of combustion [20–22] approach closest. It is not expected that mere 0D modelling of this flowing, heterogeneous plasma suffices to describe it, although methods exist to translate 0D models into models of non-uniform discharges [3].

Validation of a fluid model can be done by comparing with experimental measurement, e.g. of velocity components [23,24] or (additionally) with temperature [24]. In combustion modelling, conditions get comparable to plasma conditions, and validation of these models exists [20–22], although the maximum temperature of the microwave plasmas we describe lies between 3000 to 7000 K, while in the mentioned combustion cases the maximum temperature is about 2000 K. Validation of a microwave plasma with measured temperature has been performed in Gutsol and Bakken [6], which is based on the wall and outlet temperatures, not within the plasma or in the direct periphery, and only for air or nitrogen mixtures. In our work, we compare our modelling results with both axially and radially resolved temperature profiles (with 1 to 2 mm resolution).

The chemistry of a CO_2 plasma, in combination with its (turbulent) flow, causes the modelling to be very complex, often demanding many computational resources. In combustion modelling, ways of handling such complex chemistry have been developed through the use of chemical reduction, e.g. [25–27] although these models are still complex when combined with the fluid equations.

In this paper the gas composition is described by an effective single gas species with its properties based on those of a plasma mixture. Although it is known that the electron temperature is higher than the gas temperature in the investigated plasmas, especially at lower pressures [28], it is assumed that the different degrees of freedom, translational, rotational and vibrational, can be described by one temperature, i.e. by the gas temperature. The microwave plasma under investigation is very weakly ionised (typically in the order of 10^{-5}–10^{-4}) as has been measured by Wolf et al. [7] (see also [29]), so that electron–ion contributions are minimal and do not affect the macroscopic gaseous behaviour of these plasmas. In addition, it has been determined that the plasma can be very well described using one temperature to describe the different degrees of freedom of the molecules and atoms [28], especially in the region outside the plasma region.

In order to limit the computational demands, the two-equation Reynolds Averaged Navier–Stokes (RANS) eddy viscosity models are preferred over, more sophisticated, but more demanding models, like the Reynolds Stress equation Model (RSM; also a RANS model). The most common, well known, and relatively simple two-equation RANS models, are the k-ε, and the k-ω models [30].

Our aim is to develop a relatively simple, computationally light CFD model that best describes our forward vortex microwave plasma system, that can be used in the future to optimise a microwave plasma reactor optimised for CO_2 conversion. The model, in short, is a 3D turbulence model of a tube with two tangential gas inlets, one central outlet at the downstream side of the tube, and a heat source on the tube axis that represents the microwave heating. The simulations in this work do not solve for interactions between the microwaves and the electrons, but impose the measured plasma profile as the shape of the heat source. Its simplicity is with respect to the description of the turbulence by two-equation RANS models, and of the chemistry and composition of the mixture, which are described by a single species with effective properties, e.g. specific heat and thermal conductivity. In this heated gas then, charged particle effects are implicit in its effective properties, but are assumed negligible as explained above. In the model of its flow only the effective species is taken into account. Imaging of the plasma is used to determine the heat source profile [7]. Validation in our work is done by comparing with measured gas temperatures, and we investigate which turbulence model is best, focussing on the (near) plasma region. The question is whether such a simple model is able to describe the experimentally observed gas temperatures, in particular in the vicinity of the plasma.

In this paper, firstly the experimental setup of the forward vortex microwave plasma is described, followed by a description of the model. The results of the model are compared with the measurements of the neutral gas temperature. In summary

- We develop a computationally light gas flow (CFD) model for a forward vortex microwave CO_2 plasma.
- The plasma is represented in the model by a heated gas with
- a heat source having the shape of an experimentally observed plasma, and
- the gas being a single species gas, having “effective” properties (as a function of temperature) that are calculated beforehand using a model of a plasma mixture, including CO_2, CO, O_2, O, ions, and electrons, at the experimental gas pressure.
- Because the low degree of ionisation of the plasma, and because the degrees of freedom of the atoms and molecules can be described by a single temperature, the effects of a higher electron temperature can be neglected due to the low ionisation degree.
- The resulting temperature profiles of the CFD model are validated against measured gas temperatures.

2. Description of experiments used for model input and validation

The data used for the heated gas flow model input and validation are taken from measurements performed earlier by Wolf et al. [7]

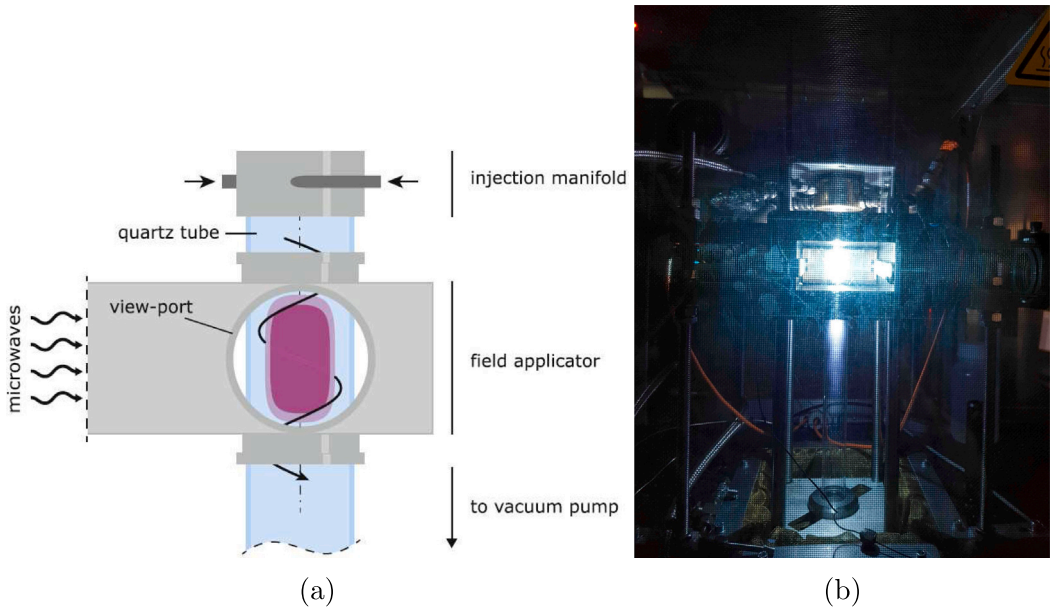

Fig. 2. (a): Schematic of the forward vortex experimental setup. (b): Experimental setup of the forward vortex with a CO_2 microwave plasma, looking into the waveguide. *Source:* Figure from [31].

and Van de Steeg et al. [28] in separate CO_2 microwave plasma experiments, for a number of experimental conditions (pressure, mass flow rate, microwave power). Details of the experiments are given in these references. In the following, first the microwave reactor and then the experiments are described.

The 2.45 GHz microwave plasma reactor utilises a straight quartz tube (inner diameter $\varnothing_{in}$ = 27 mm, 350 mm length) that penetrates perpendicularly the wide side of the WR340 waveguide (width 86.36 mm, height 43.18 mm). Mounted on the tube is a metal injection manifold that has two tangential inlets ($\varnothing_{in}$ = 2.5 mm, 15 mm length each). The axes of the tangential inlets lay 5 mm away from the closed top of the tube. See Fig. 2(a).

The spatially resolved temperature measurements used for validation of the model have been performed using Raman scattering [28] and Doppler broadening [7]. The Raman scattering based temperature measurements have used laser-based rotational Raman spectroscopy of molecular CO_2, CO, O_2, and atomic O [28]. A frequency-doubled Nd:YAG laser is focused into the reactor, and the scattered light is led to a spectrometer [28], see Fig. 3(a). The Doppler broadening based measurements have used Doppler broadening of the optical emission profiles of the 777 nm oxygen triplet emission, using a 3.3 pm resolution f = 2.25 m spectrometer in Littrow configuration [31], see Fig. 3(a).

Four combinations of input power, mass flow rate, and pressures have been measured, namely 100 mbar and 250 mbar at 860 W, 12 slm on the one hand, and 60 mbar and 120 mbar at 1000 W, 10 slm on the other. The Raman scattering diagnostic is not suitable for higher pressures than about 120 mbar and temperatures greater than, roughly, 5000 K, when formation of carbon starts [32]. The Doppler broadening diagnostic, however, is suitable for these higher pressures and temperatures. The temperatures for the 1000 W cases have been obtained with Raman scattering and for the 860 W cases they have been obtained from Doppler broadening.

Both with Raman scattering and Doppler broadening, 2D temperature profiles have been measured. With Raman scattering, the radial profile ranges from 0 to 10 mm from the plasma centre (resolution of 1 mm). These radial measurements have been performed for positive y values, and axial symmetry is assumed [19,28]. The axial profile has been measured at multiple axial positions between z = 0.046 m i.e. upstream, to z = 0.204 m downstream of the plasma centre (resolution of 2 mm), with z=0 m defined at the top of the tube. The axial measurement range is larger than the height of the waveguide. See Fig. 3(b). The uncertainty in the measurement for this method increases with decreasing density. With Doppler broadening the temperature profile has been measured in a smaller spatial area. The radial profile ranges from 0 to 3 mm (resolution of 1 mm) and from 0 to 6 mm (resolution of 2 mm) from the plasma centre. The axial profile ranges from z = 0.083 m to z = 0.117 m (resolution of 4.25 mm) upstream and downstream of the plasma centre respectively, with z = 0 m defined at the top of the tube, see Fig. 3(b). The axial measurement range is therefore smaller (i.e. mainly the peak only) than for Raman scattering, and lies within the waveguide height. The uncertainty in the measurement for this method was found to be an absolute error of 500 K.

The model input taken from the experiments are tube geometry, input power, pressure, mass flow rate and plasma shape (i.e. the axial and radial widths). The shape of the plasma is approximated by both a Gaussian axial, and Gaussian radial distribution, for our pressure, mass flow rate and power regimes [7,31]. The widths and amplitude of this 'Gaussian ellipsoid' shape of the plasma have been measured and fitted, based on the emission intensity profile of atomic oxygen at 777 nm. This transition is mostly populated by electronic impact excitation and the emission intensity scales with the electron density [7]. The power density profile, i.e. the shape of the heat source, is described by this intensity profile. The proportionality of the power density to the emission intensity is described in Wolf et al. [31], and in turn the proportionality of the intensity to the electron number density in [7]. Examples of the O emission intensity profiles for 100 mbar and 250 mbar are given in Fig. 4.

An overview of the conditions (power, pressure, and CO_2 mass flow rate) as well as the measured shapes, is given in Table 1.

More conditions have been studied and are not shown here, but are given in S3. Is should also be noted that Raman measurements have provided us also with the plasma composition.

3. Model

The effective properties of the gas are calculated prior to the flow simulations, using PLASIMO [33], so that in the former no chemistry

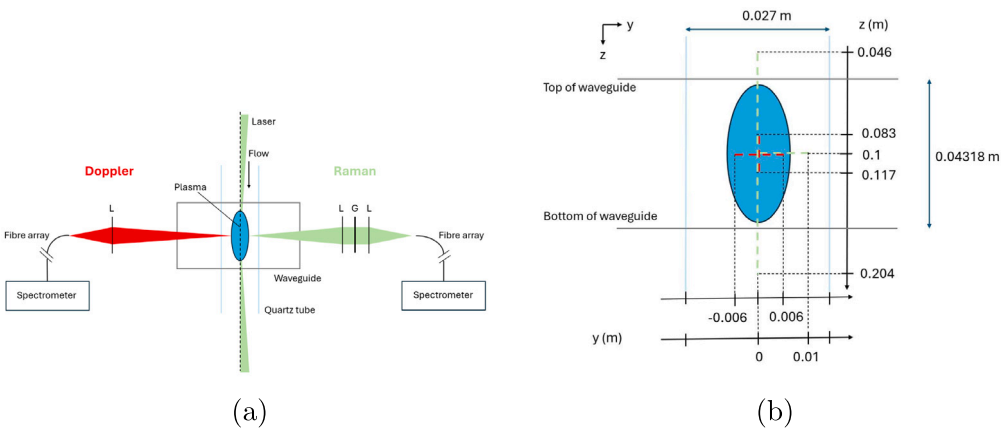

Fig. 3. (a): A combined cartoon of the temperature measurement setups using Doppler broadening as done by Wolf et al. [7], and using Raman scattering as done by Van de Steeg et al. [28]. L denotes a lens, G is a volume Bragg grating. In the case of the Raman scattering the top of the tube is optically opened for the laser. The plasma is centred at the waveguide.
(b): A schematic impression of the plasma (the ellipsoid) and the (y:"radial", z:"axial") ranges in which the temperature has been measured at various positions (not to scale). The plasma is centred at the waveguide, with its peak positioned at z = 0.1 m (the top of the tube, not shown, being the reference point for z = 0 m), and y = 0 m is on axis. The range of Doppler broadening measurements (in red) lies between y = −0.006 m and y = 0.006 m (100 mbar), and y = −0.003 m and y = 0.002 m (250 mbar), and between z = 0.083 m and z = 0.117 m. The axial range lies within the waveguide height. Positions near and parallel to the axis (y = 0.002 m) and diametrical positions near z = 0.1 m (z = 0.10425 m) used as an error estimate (described in the results section) are not shown for clarity.
The range of Raman scattering measurements (in green) lies between y = 0 m and y = 0.01 m, and between z = 0.046 m and z = 0.204 m. Axial symmetry is assumed. The axial range exceeds the waveguide height.

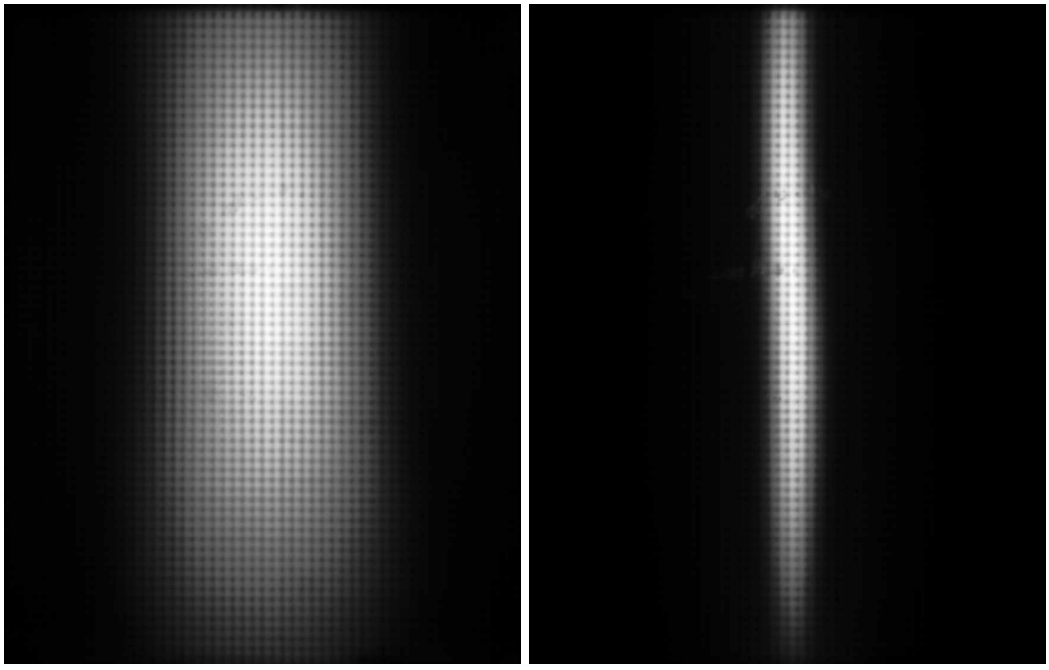

Fig. 4. O emission intensity profiles at 12 slm, 870 W (a): 100 mbar. (b): 250 mbar.The meshed pattern is from the observation window in the waveguide.

calculations are necessary. The calculations of the 3D swirling flow models have been performed with ANSYS Fluent [34]. We want to remark explicitly here that a model based on a pure CO_2 gas, as provided by default by ANSYS Fluent, with some slightly tweaked properties (e.g. using an extrapolated Sutherland viscosity) could not produce any satisfactory results.

The CO_2 plasma mixture (of CO_2, CO, O_2, and O, as well as their associated ions, and electrons) and its effective transport and thermodynamic properties are calculated, as a function of temperature, with PLASIMO [33]. In this PLASIMO CO_2 model the following quantities are calculated [35], assuming one temperature, T. The gas composition is calculated by minimisation of the chemical potential. In the model's calculation, particle number densities follow directly from the temperature. The specific heat (including the 'frozen', i.e. non-reactive, and reacting contributions) is calculated from the temperature derivative of the enthalpy (which is calculated from the number density, formation energy, temperature, the partition sum, and its first moment). The viscosity is calculated using the Chapman–Enskog method. The thermal conductivity consists of four terms: the heavy particle translational, electron translational, reactive, and internal terms. The reactive thermal conductivity reflects the phenomenon that chemical reactions in gas mixtures increase the thermal conductivity. Concentration gradients, caused by temperature variations, lead to diffusion of molecules

Table 1
Plasma power density profiles' axial and radial widths.

860 W, 12 slm CO_2		
p (mbar)	$FWHM_z$ (mm)	$FWHM_r$ (mm)
100	22	7.2
250	24	2.1
1000 W, 10 slm CO_2		
p (mbar)	$FWHM_z$ (mm)	$FWHM_r$ (mm)
60	27	9.5
120	21	2.7

that transport additional heat as chemical enthalpy (when a molecule that dissociates in a high temperature region, diffuses to a lower temperature region, and reassociates there) [36]. The contribution of electrons and ions to these gas transport coefficients is neglected for the studied plasma, as explained in the introduction. For further details of the PLASIMO model, see [35].

These gas properties are fitted with piecewise polynomials of the temperature over a number of temperature regions, compatible with ANSYS Fluent. All properties are lumped in the effective species. Note that the contribution of the charged particles are in this way implicitly taken into account in the effective gas properties. Using such a reduction in the model, i.e. no calculation of kinetics, explicit chemistry or reactions, is beneficial for its computational performance. This assumes, however, instantaneous behaviour as function of temperature, e.g. dissociation and recombination happen instantly (implicitly in the properties) at their characteristic temperatures with zero reaction time. See Fig. 5 for examples of gas properties of the 60 mbar and 120 mbar cases. The two peaks in the figure of C_p at about 3000 K and 6500 K correspond to the dissociation of CO_2 and CO respectively, see also [31]. When the CO_2 molecule dissociates, the heat that is added to the plasma is then no longer put in the internal degrees of freedom of that molecule, but rather in the kinetic energy of the dissociation products that have less internal degrees of freedom. This dissociation also leads to an increase of the reactive thermal conductivity, which causes the peaks in the total thermal conductivity.

The heat source power density profile is described as follows:

$$\mathcal{P}(r,z) = \mathcal{P}_0 \exp(-r^2/(2\sigma_r^2)) \exp(-(z-z_0)^2/(2\sigma_z^2)), \quad (1)$$

where $\mathcal{P}_0$ is a factor that is chosen such that the volume integral over the distribution is equal to the total input power, $r^2 = (x^2+y^2)$, σ_r and σ_z are the radial and axial standard deviations respectively, z corresponds to the axial direction, and z_0 is the axial peak position. Note that the microwave field itself is not a directly modelled quantity, but its power is taken into account through this heat source term.

Having the gas properties and the heat source for the heated gas defined, the flow in ANSYS Fluent is solved using the widely applicable pressure-based solver with the default, yet robust, SIMPLE scheme [34]. Additionally, for the turbulent flow, a two-equation RANS model is used. The most well known two-equation RANS models are the k-ε and the k-ω models. Roughly speaking, originally the k-ε model is known to perform better in free shear flow, and flow is assumed fully turbulent [30,34], while the k-ω model suits better for near-wall modelling [30]. In these models k is the turbulent kinetic energy (per unit mass) of the velocity fluctuations, at a given location. The quantity ε is the rate of dissipation (into thermal energy) of the turbulent kinetic energy (per unit mass), i.e. a destruction term of the turbulent kinetic energy. Equivalent to ε is $\omega = \varepsilon/k$ the specific rate of dissipation (i.e. the dissipation rate per unit turbulent energy), also called the turbulence frequency, since it has the dimension of reciprocal time. Since the fluctuations are unknown, k, ε, and ω are solved using transport equations. For more details, see [30,34,37], and the supplementary information S1.

Table 2
Boundary conditions of the fluid model [34]. The equation for q of the wall corresponds to the combined (or mixed) thermal boundary condition. The user defined values for the shown results are also given. See the text for more details.

Boundary	Equation(s)	Description
inlet 1	$\rho\vec{v} = \frac{\dot{m}}{A}\vec{n}$, T	Mass-Flow Inlet
	$\dot{m}$ = 10 and 12 slm CO_2 ; T = 300 K	
inlet 2	(idem)	(idem)
outlet	p, T	Pressure Outlet
	p = 60, 100, 120 and 250 mbar ; T = 300 K	
wall	$q = h_f(T_w - T_f) + q_{rad}$	Stationary Wall, No Slip, Combined external heat transfer condition
	$= h_{ext}(T_{ext} - T_w) + \varepsilon_{ext}\sigma(T_\infty^4 - T_w^4)$	
	h_{ext} = 2000 W m^{-2} K^{-1} ; T_{ext} = 300 K ; ε_{ext} = 0.9 ; T_∞ = 300 K	

Although the standard k-ε model is regarded as the 'workhorse of practical engineering flow calculations' [34], it is in principle insensitive to the streamline curvature and not suitable for swirling flow. Other k-ε models can take care of this, e.g. the RNG k-ε and realisable k-ε models [34]. Also a curvature correction (abbreviated to 'cuco' below) can be added to the standard k-ε model, which is in fact a modification of the turbulent production term [34]. This offers a possible compensation for the isotropy of the two-equation RANS models. The equations that ANSYS Fluent solves are given in the supplementary information, S1.

The following boundary conditions are used, see Table 2. Both inlets have a mass flow rate inlet boundary condition (that allows to vary the calculated pressure at the inlet) with $\dot{m}$ the (user defined) mass flow rate (in kg/s), from which the velocity $\vec{v}$ is computed (with ρ the mass density, $\vec{n}$ the normal vector). The inlet (user defined) temperature T is set at 300 K. The outlet has a pressure boundary condition (fixing the pressure at the outlet), with p the (user defined) pressure corresponding to the measured pressure, and for which the temperature is also set at 300 K. The tube wall has a no slip condition, and a "mixed" thermal boundary condition for q, the heat flux to the wall, with h_f the fluid-side local heat transfer coefficient, T_w the wall surface temperature, T_f the fluid temperature, q_{rad} the radiative heat flux, h_{ext} the (user defined) external heat transfer coefficient, set to 2000 W m^{-2} K^{-1}, T_{ext} the (user defined) external heat-sink temperature, set to 300 K, ε_{ext} the (user defined) emissivity of the external wall surface, set to 0.9, σ the Stefan–Boltzmann constant, T_∞ the (user defined) temperature of the radiation source or sink on the exterior of the domain, set to 300 K [34].

The model is represented in a model structure diagram in S1.

4. Results and discussion

For our modelling purpose the k-ε, and k-ω models have been investigated. Although the limitations of the standard k-ε model are known, it serves as a reference case. Also the curvature correction has been switched on for the standard k-ε model to see its effect. Our main observable is temperature, so we will investigate temperature related features. These features can be related to both flow (e.g. turbulent thermal conductivity and advection), and to the gas thermodynamic, and transport properties of the gas that describes the plasma. Specifically, concerning the flow pattern, we are interested in the axial (forward) velocity, and the turbulent kinematic viscosity ν_t. The axial velocity is a measure of how fast heat is advectively transported to the exhaust. This will then also include the presence, and size, of the recirculation cell, which opposes the transport to the exhaust, and, moreover, enables gas from the outer vortex zone to (re-)enter. The turbulent viscosity ν_t is a direct measure of the contribution of the turbulence to the thermal conductivity (via S1 equation 11). The gas properties of interest are

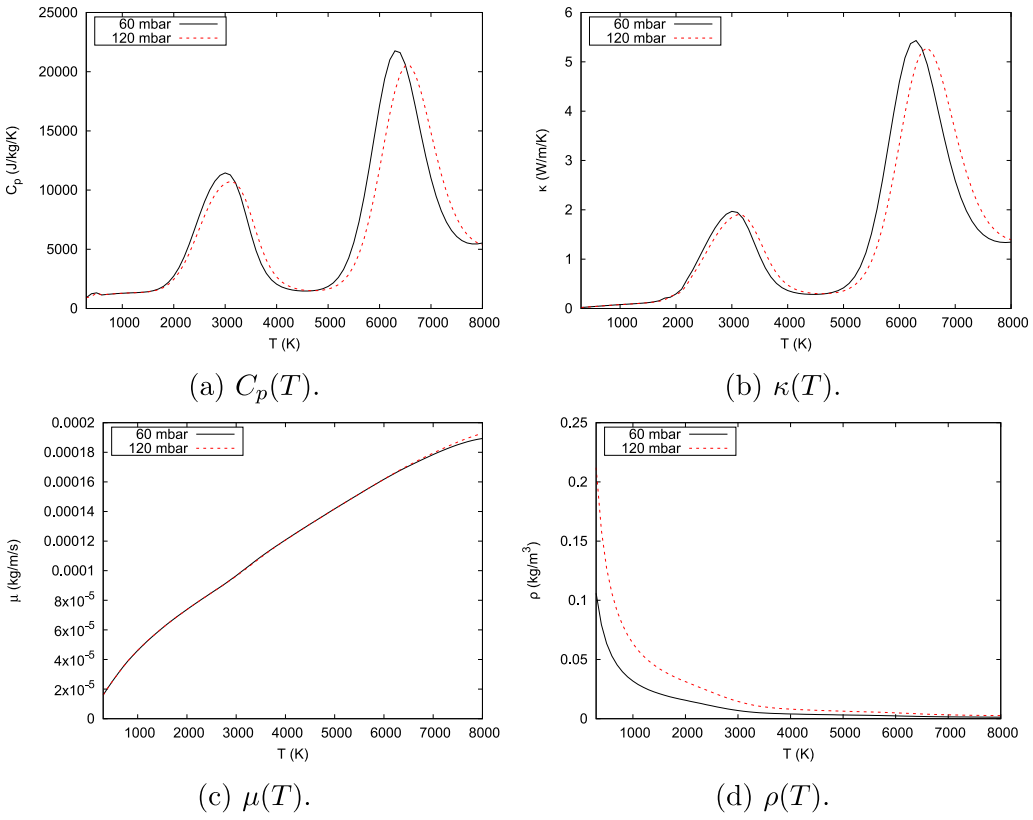

Fig. 5. Gas properties as function of temperature, at 60 and 120 mbar. Output from the PLASIMO CO_2 model, with C_p the specific heat capacity at constant pressure, κ the thermal conductivity, μ the dynamic viscosity, and ρ the mass density.

the specific heat (which also contributes to the turbulent thermal conductivity), and thermal conductivity. Together these contribute to the resulting temperature profile in the models, which can be compared to the experimentally measured profiles.

4.1. Model validation

In this section the heated gas models are compared with the experimentally obtained temperature profiles at 1000 W, 60 and 120 mbar, and at 860 W, 100 and 250 mbar. For all results presented here grid convergence has been investigated; the result for one particular case, the 60 mbar, 10 slm, 1000 W, k-ω model, is given in the supplementary information, S3.

The radial and axial temperature profiles for model and Raman scattering (10 slm CO_2) at 60 mbar and 120 mbar are shown in Figs. 6 and 7, respectively. Fig. 6 also shows the various k-ε models. Although the RNG and realisable k-ε models, as well as the k-ε model with curvature correction ('cuco'), show better agreement with measurement than the standard k-ε model, it shows that the k-ω model shows the best agreement with experiment. This is the case for all other conditions as well, so from here on we only focus on the results for the k-ω model. It can be seen in Fig. 7 (120 mbar) that there is even better agreement upstream and further downstream from the heated zone. The 60 mbar case shows better agreement at the peak than the 120 mbar case. Both cases, however show that the models' temperatures do not agree with the measurements immediately downstream from the heated zone, although for 120 mbar this agreement is much better.

Fig. 8 shows the modelled and measured temperature profiles for 100 mbar and 250 mbar, as measured with Doppler broadening. To get an idea of the temperature dependency on position (acting like an uncertainty measure for the model), the measured radial profiles are shown at the peak position (z = 0.1 m) and a small displacement downstream of 4.25 mm, while the measured axial profiles are shown on axis (y = 0 mm) and a small displacement off axis of 2 mm.

It can be seen that both temperature profiles agree very well, but that in the 100 mbar case the peak temperature is overestimated, and radially the gradient is underestimated somewhat.

Fig. 9 shows the 2D profiles of the axial velocity, and an indication of the recirculation cell boundary (black dots) for the 60 mbar, and 120 mbar, 10 slm cases. The appearance of a recirculation cell causes gas to longer reside in the heated zone, increasing the possibility of dissociation. Downstream of the plasma and of the recirculation zone, the axial forward velocity tends to be somewhat higher next to the tube axis, than on the axis. The gas that swirls forward at the edges around the recirculation zone, i.e. near the wall, is able to reach this zone where the forward velocity is higher, so that it relatively quickly reaches the exhaust.

Fig. 10 shows that the kinematic turbulent viscosity ν_t is higher upstream and near the inlets, than it is downstream, so that turbulent behaviour affects the flow mainly upstream.

Temperature deviations could be caused by an overestimation of the heat transfer through the wall. Therefore the role of the wall heat loss on the heated region has been investigated by altering the heat transfer coefficient h_{ext} (see the boundary condition description in the model Section 3) which was varied between 10 and 2000 $W\,m^{-2}\,K^{-1}$ (with a free stream temperature T_{ext} and external radiation temperature T_∞ of 300 K, an external emissivity ε_{ext} of 0.9, and wall thickness of 0.0015 m). Near the wall, the model is sensitive to this change, but not in the heated region, where our focus lies. This is in line with the better heat confinement in this heated region.

Summarising this section, we see that the k-ω modelling method is applicable, but that there are deviations mainly downstream from the heated zone. The lack of agreement with experiment for the k-ε implies that the flow in our reactor is surface determined, rather than fully turbulent. The 120 mbar case agrees best, but the model

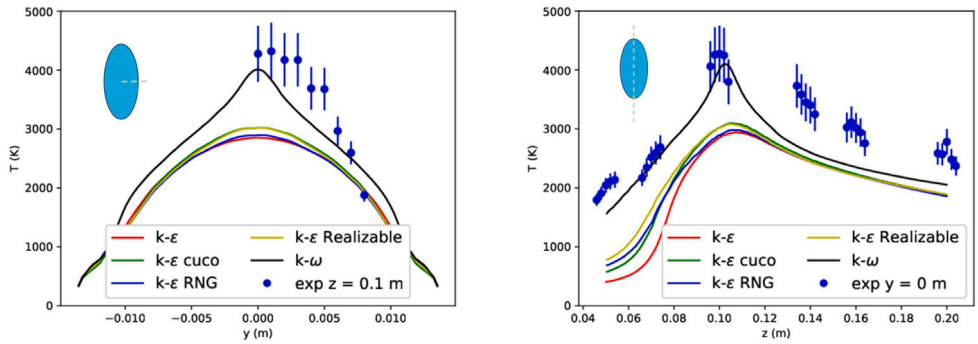

(a) Temperature on diameter (z=0.1 m). (b) Temperature on tube axis (y=0 m).

Fig. 6. Temperature for model and experiment (Raman scattering), 1000 W, 10 slm, and 60 mbar. The radial measurements have been performed for positive y values, and axial symmetry is assumed [19,28]. On diameter corresponds to z = 0.1 m. On axis corresponds to y = 0 m. (For interpretation of the references to colour in this figure legend, the reader is referred to the web version of this article.)

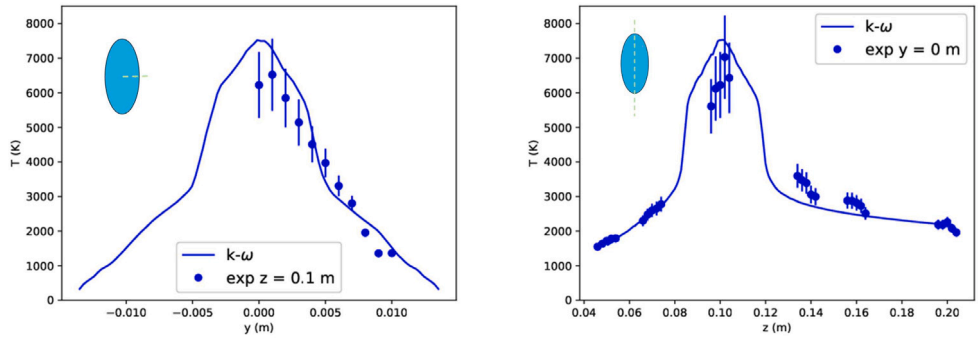

(a) Temperature on diameter (z=0.1 m). (b) Temperature on tube axis (y=0 m).

Fig. 7. Temperature for model and experiment (Raman scattering), 1000 W, 10 slm, and 120 mbar. On diameter corresponds to z = 0.1 m. On axis corresponds to y = 0 m.

works less well for 60 mbar (downstream) and 100 mbar (at the peak). Therefore, in the following subsection, we explore the model's sensitivity to variation of the input parameters, and investigate its deviation from the experimental result.

4.2. Sensitivity analysis: improving the model

The underestimation of the downstream temperature in the 1000 W, 60 mbar, 10 slm model (no downstream measurements for 100 mbar and 250 mbar) is expected to be caused by a stronger deviation from the gas composition as calculated with the PLASIMO model, see figure 1a in S2. To investigate this deviation, two parameters directly related to the temperature have been changed individually. The first parameter is the turbulent Prandtl number (called the Energy Prandtl number in ANSYS Fluent), defined via $\kappa_t = C_p \mu_t / \mathrm{Pr_t}$ (S1, Eq. 11). This scaling factor, which is related to the specific heat, turbulent viscosity μ_t, and turbulent thermal conductivity, is a constant of the (turbulent) model that is not known a priori for our gas. ANSYS Fluent uses a default value of 0.85. (Investigation of sensitivity to changes in the specific heat, and the thermal conductivity individually are shown in supplementary information S3.) The second parameter is the shape, i.e. the radial and axial width, of the heat source; a main input of the model. We want to know the sensitivity of the model to this input, since the actual power density profile is not exactly known.

4.2.1. Sensitivity to turbulent prandtl number

Fig. 11 (radial and axial profile) shows the sensitivity of the modelled temperature profiles to changes in the turbulent Prandtl number for the 1000 W, 60 mbar, 10 slm case. (See S3 for the radial profile at an 'upstream' z position, z = 0.05 m.) Increasing $\mathrm{Pr_t}$ results in a temperature profile that better matches the measured one in the upstream part of the tube, where the turbulence is strongest. A higher $\mathrm{Pr_t}$ implies a smaller turbulent heat transfer as compared to the turbulent viscosity and specific heat, so that the original model overestimated the turbulent thermal conduction (and/or underestimated the product of C_p and μ_t) in this part of the tube. For 60 mbar a $\mathrm{Pr_t}$ value between the default 0.85 and 3 is recommended, though the default value is already suitable for modelling the plasma region.

Since the plasma region temperature in the k-ω model for the 100 mbar, 12 slm, 860 W case is overestimated in the model, we investigate the effect of changing $\mathrm{Pr_t}$ for this condition as well. The result is shown in Fig. 12. A $\mathrm{Pr_t}$ value of about 0.5 to 0.6 gives much better agreement with the measured values. A lower turbulent Prandtl number implies a higher contribution of turbulent thermal conductivity than at other conditions. The difference with e.g. the case of 60 mbar, 10 slm, 1000 W, is likely to be found in the gas composition: for both cases the peak temperature is about 4000 K, so when using the effective species, both models assume very similar gas composition. In reality, however, the gas composition differs significantly for these two conditions (see S2). This difference can be accounted for in the model by adjusting the turbulent Prandtl number instead.

4.2.2. Sensitivity to power density profile

Fig. 13 (radial and axial profile) shows the sensitivity of the temperature profiles to changes in the width of the heat source for the 1000 W, 60 mbar, 10 slm case. (See S3 for the radial profile at an 'upstream' z position, z = 0.05 m.) These changes of the shape have been investigated by varying the axial FWHM, leaving the radial FWHM constant, and vice versa. The peak temperature is affected significantly by deviations from the measured FWHMs (FWHM_r = 9.5 mm, and

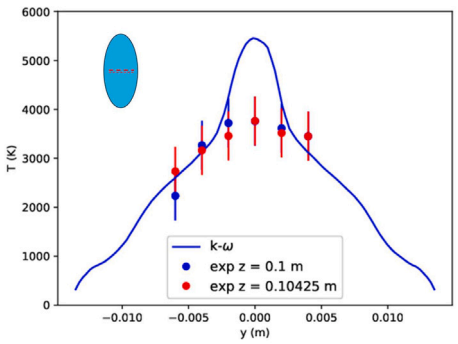

(a) Temperature on diameter, 100 mbar.

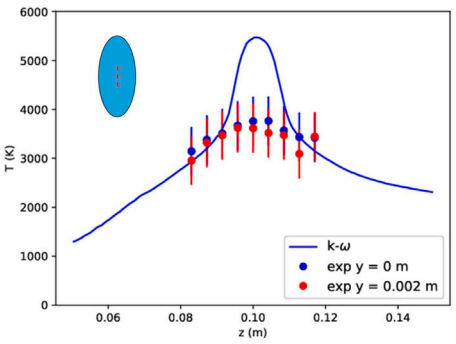

(b) Temperature on tube axis, 100 mbar.

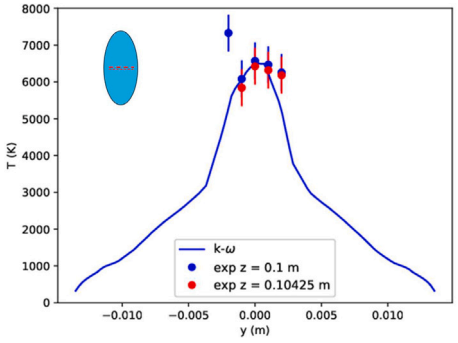

(c) Temperature on diameter, 250 mbar.

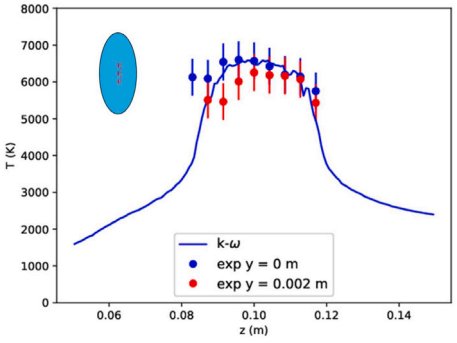

(d) Temperature on tube axis, 250 mbar.

Fig. 8. Temperature for model and experiment (Doppler broadening), 860 W, 12 slm, 100 mbar, and 250 mbar. On diameter corresponds to z = 0.1 m. The experimental values for z = 0.10425 m are also shown to give a measure of the uncertainty. On axis corresponds to $y = 0$ m; the $y = 0.002$ m results are also shown as an uncertainty measure. (For interpretation of the references to colour in this figure legend, the reader is referred to the web version of this article.)

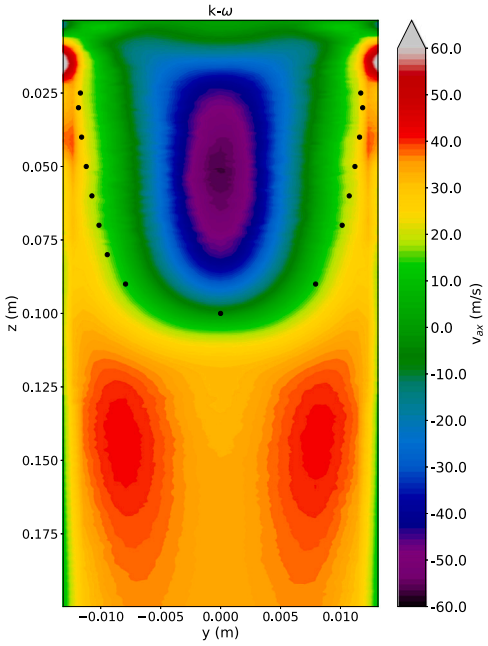

(a) 60 mbar.

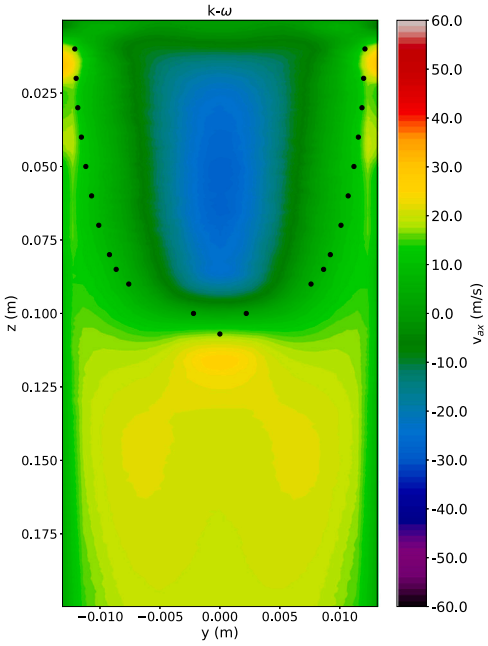

(b) 120 mbar.

Fig. 9. Axial velocity 2D profiles, 1000 W, 10 slm using the *k-ω* models. The flow is from top to bottom. The recirculation cell boundaries are shown for a number of axial positions (black dots). (For interpretation of the references to colour in this figure legend, the reader is referred to the web version of this article.)

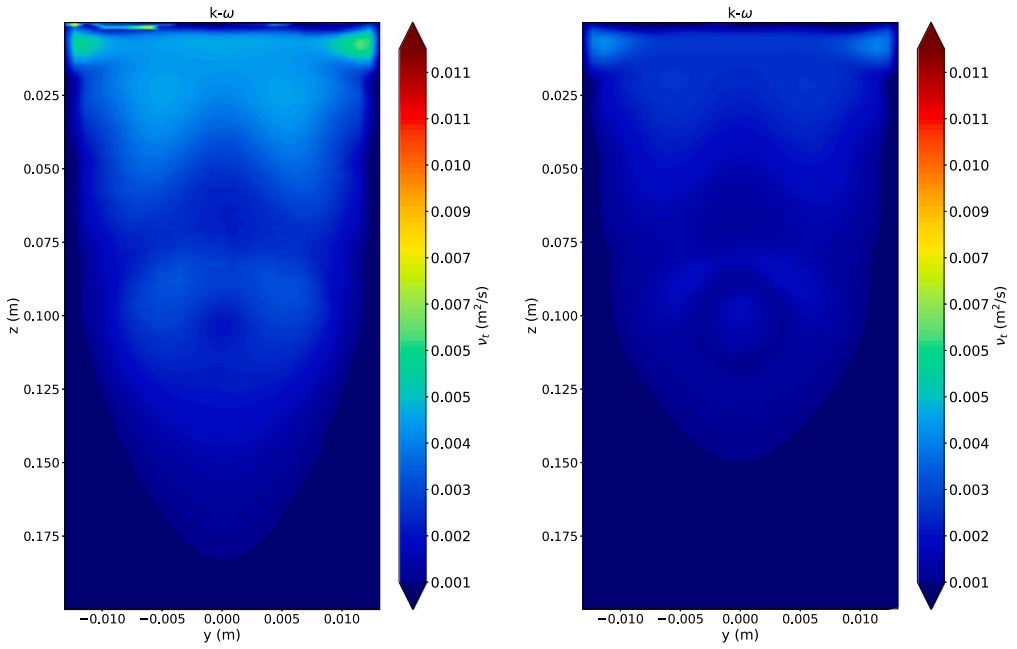

(a) 60 mbar. (b) 120 mbar.

Fig. 10. Turbulent kinematic viscosity (ν_t) 2D profiles, 1000 W, 60 and 120 mbar, 10 slm. (For interpretation of the references to colour in this figure legend, the reader is referred to the web version of this article.)

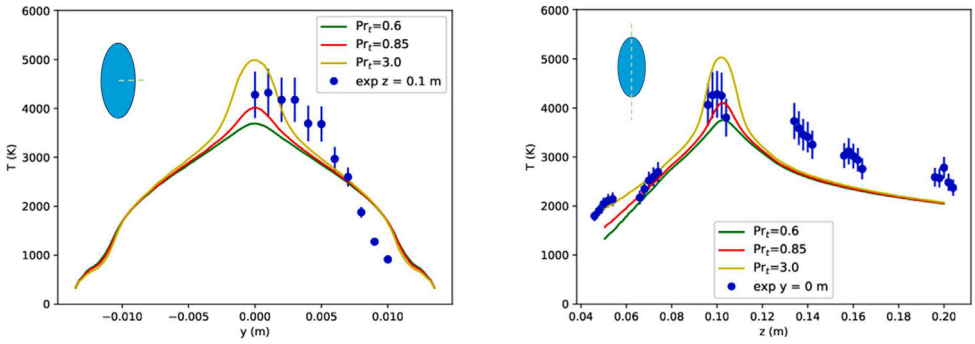

(a) Temperature on diameter (z=0.1 m). (b) Temperature on tube axis (y=0 m).

Fig. 11. Temperature for model and experiment (Raman scattering), 1000 W, 10 slm, and 60 mbar. In the model the turbulent Prandtl number has been varied. (Default: Pr_t = 0.85.) On diameter corresponds to z = 0.1 m. On axis corresponds to y = 0 m. A Pr_t between the default value and 3 is recommended. (For interpretation of the references to colour in this figure legend, the reader is referred to the web version of this article.)

$FWHM_z$ = 27 mm), especially for the radial width. This has a major effect on the peak temperature, and not on other parts of the temperature profile.

Varying the axial position of the heat source only shifted the temperature profile, but not its shape or height.

Fig. 14 shows that for the 100 mbar case (for which only the radial width is changed), the peak temperature in the model is very sensitive to changes in the radial width (measured $FWHM_r$ = 7 mm).

So, the peak temperature, and to some extent the profile, can be matched to measurement by changing the turbulent Prandtl number, and by narrowing, the shape of the power density source. The resulting upstream temperature can be improved especially by increasing the turbulent Prandtl number in the 60 mbar case, and decreasing it in the 100 mbar case. The downstream temperature could not be matched, and the model underestimated the temperature there. In the model the gas composition is directly coupled to the local temperature, while in reality this is not the case, because composition is based on the upstream 'history'. So the gas composition assumption is expected to fail, especially downstream and at low pressures, where there is less recombination and equilibration of the chemistry with temperature.

5. Conclusions and outlook

In this paper it has been shown that a relatively simple RANS two-equation k-ω turbulent flow model is able to describe the experimentally observed temperature in the plasma region. We summarise our additional conclusions as follows:

- Prominent deviations occur downstream, especially for the 60 mbar case, likely due to the calculated gas composition used to determine the single effective species becoming invalid (the downstream mixture being CO and O rich in reality, while almost entirely CO_2 in the model).

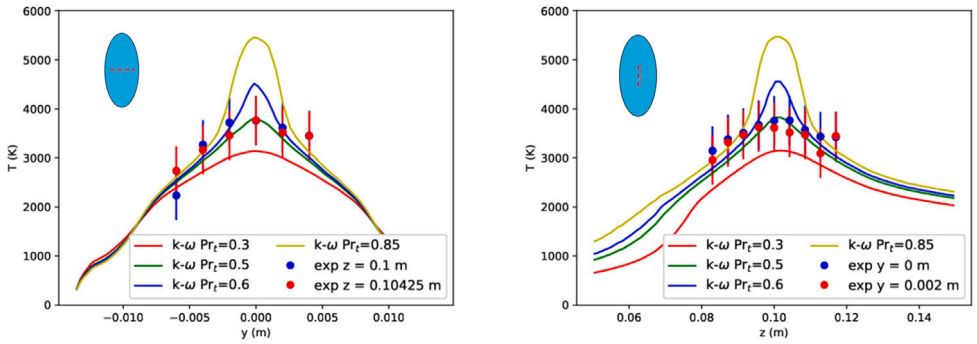

(a) Temperature on diameter (z=0.1 m). (b) Temperature on tube axis (y=0 m).

Fig. 12. Temperature for model and experiment (Doppler broadening), 860 W, 12 slm, and 100 mbar. In the model the turbulent Prandtl number has been varied. (Default: Pr_t = 0.85.) On diameter corresponds to z = 0.1 m. The experimental values for z = 0.10425 m are also shown to give a measure of the uncertainty. On axis corresponds to y = 0 m; the y = 0.002 m results are also shown as an uncertainty measure. A Pr_t between 0.5 and 0.6 is recommended. (For interpretation of the references to colour in this figure legend, the reader is referred to the web version of this article.)

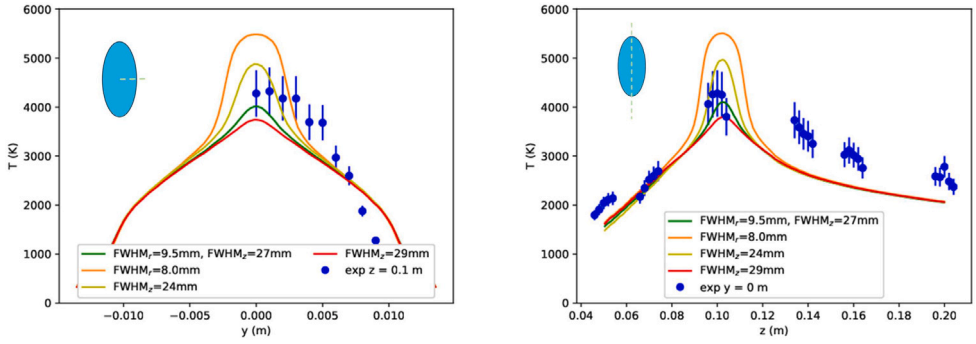

(a) Temperature on diameter. (b) Temperature on tube axis.

Fig. 13. Temperature for model and experiment (Raman scattering), 1000 W, 10 slm, and 60 mbar. In the model the axial and radial widths of the heat source have been varied. (Measured $FWHM_z$ = 27 mm, $FWHM_r$ = 9.5 mm.). (For interpretation of the references to colour in this figure legend, the reader is referred to the web version of this article.)

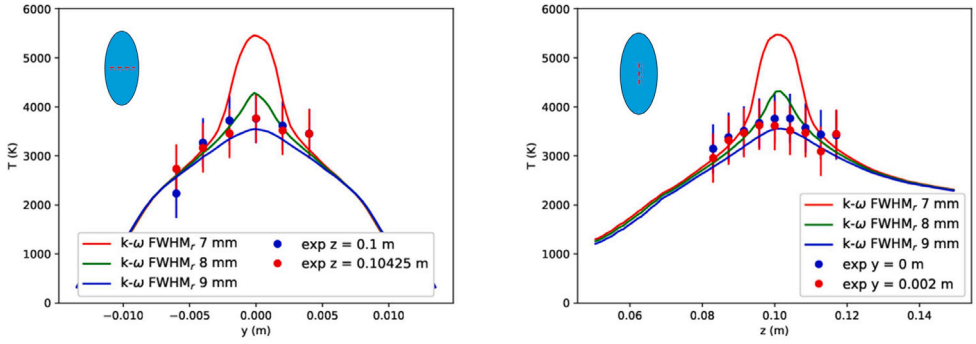

(a) Temperature on diameter. (b) Temperature on tube axis.

Fig. 14. Temperature for model and experiment (Doppler broadening), 860 W, 12 slm, and 100 mbar. In the model the radial width of the heat source has been varied. (Measured $FWHM_r$ = 7 mm.). (For interpretation of the references to colour in this figure legend, the reader is referred to the web version of this article.)

- The, as yet unknown, turbulent Prandtl number in high temperature CO_2 plasma can be set to the default value of Pr_t = 0.85, which is suitable in the plasma region at low pressures (60 mbar) and higher pressures (250 mbar).
- At intermediate pressures (around 100 mbar) the turbulent Prandtl number requires adjustment down to Pr_t = 0.5 from the default of Pr_t = 0.85. This adjustment is likely required due to the model, that calculates the effective gas, not adequately describing the plasma composition at this pressure.
- Alternatively, a slight adjustment of the radial FHWM in the power density profile from $FWHM_r$ = 7 mm to $FWHM_r$ = 8 mm at pressures of 100 mbar also significantly improves correspondence of the model with experiment without adjusting Pr_t.

Self-consistently modelling the coupling of the microwave field with the electrons, and bypassing the need for experimentally determining the power density profile as an input to the model, would allow for e.g. establishing the correct value of the turbulent Prandtl number in high temperature CO_2 plasma. Incorporating non-equilibrium

behaviour is also recommended, e.g. see [3,38], as well as more sophisticated turbulent flow modelling, incorporating anisotropic turbulent conduction (e.g. the Reynolds Stress equation Model (RSM) [39]). For both of these options, however, computation becomes significantly more intensive, while we have shown that with a relatively simple k-ω turbulence model, we are able to reproduce the temperature profiles. This good agreement of our model with experiment in the plasma region of the forward vortex microwave CO_2 plasma, is a good starting point for investigating other geometries, other plasma conditions, and other plasma compositions.

CRediT authorship contribution statement

P.W.C. Groen: Writing – review & editing, Writing – original draft, Validation, Methodology, Investigation, Conceptualization. **W.A. Bongers:** Writing – original draft, Supervision, Resources, Conceptualization. **J.F.J. Janssen:** Writing – original draft, Software, Resources. **T.W.H. Righart:** Writing – original draft, Resources, Investigation. **A.W. van de Steeg:** Writing – original draft, Resources, Investigation. **A.J. Wolf:** Writing – review & editing, Writing – original draft, Resources, Investigation. **M.C.M. van de Sanden:** Writing – review & editing, Writing – original draft, Supervision, Conceptualization. **F.J.J. Peeters:** Writing – review & editing, Writing – original draft, Supervision, Resources, Conceptualization.

Declaration of competing interest

The authors declare that they have no known competing financial interests or personal relationships that could have appeared to influence the work reported in this paper.

Acknowledgements

This work was part of the Power-to-Gas (P2G) research programme with project number 15325, which is co-financed by the Netherlands Organisation for Scientific Research (NWO) and Alliander N.V.

Appendix A. Supplementary data

Supplementary material related to this article can be found online at https://doi.org/10.1016/j.cej.2024.158072.

Data availability

Data will be made available on request.

References

[1] R. Snoeckx, A. Bogaerts, Plasma technology - a novel solution for CO_2 conversion? Chem. Soc. Rev. 46 (2017) 5805, http://dx.doi.org/10.1039/C6CS00066E.
[2] W. Bongers, et al., Plasma Proc. Polym. 14 (2017) e1600126, http://dx.doi.org/10.1002/ppap.201600126.
[3] L.D. Pietanza, et al., Eur. Phys. J. D (2021) 75–237, http://dx.doi.org/10.1140/epjd/s10053-021-00226-0.
[4] G. Trenchev, et al., Plasma Sources Sci. Technol. 25 (2016) 035014, http://dx.doi.org/10.1088/0963-0252/25/3/035014.
[5] C.S. Kalra, Y.I. Cho, A. Gutsol, A. Fridman, Rev. Sc. Instrum. 76 (2005) 025110, http://dx.doi.org/10.1063/1.1854215.
[6] A. Gutsol, J.A. Bakken, J. Phys. D: Appl. Phys. 31 (1998) 704–711, http://dx.doi.org/10.1088/0022-3727/31/6/018.
[7] A.J. Wolf, T.W.H. Righart, F.J.J. Peeters, P.W.C. Groen, M.C.M. van de Sanden, W.A. Bongers, Plasma Sources Sci. Technol. 28 (2019) 115022, http://dx.doi.org/10.1088/1361-6595/ab4e61.
[8] T. Fleisch, Y. Kabouzi, M. Moisan, J. Pollak, E. Castãos-Martínez, H. Nowakowska, Z. Zakrzewski, Plasma Sources Sci. Technol. 16 (2007) 173–182, http://dx.doi.org/10.1088/0963-0252/16/1/022.
[9] W. Peng, A.C. Hoffmann, P.J.A.J. Boot, A. Udding, H.W.A. Dries, A. Ekker, J. Kater, Powder Technol. 127 (2002) 212–222, http://dx.doi.org/10.1016/S0032-5910(02)00148-1.
[10] H. Khazaei, A.R. Teymourtash, M. Malek-Jafarian, Sci. Iran. B 19 (3) (2012) 454–462, http://dx.doi.org/10.1016/j.scient.2012.03.003.
[11] T. Parra, R. Perez, M.A. Rodriguez, F. Castro, R.Z. Szasz, A. Gutkowski, J. Fluid Flow Heat Mass Transf. 2 (2015) 1–6, http://dx.doi.org/10.11159/jffhmt.2015.001.
[12] E.R. Mercer, et al., Fuel 334 (2023) 126734, http://dx.doi.org/10.1016/j.fuel.2022.126734.
[13] S. van Alphen, et al., Chem. Eng. J. 462 (2023) 142217, http://dx.doi.org/10.1016/j.cej.2023.142217.
[14] A.J. Wolf, F.J.J. Peeters, P.W.C. Groen, W.A. Bongers, M.C.M. van de Sanden, J. Phys. Chem. C 124 (2020) 16806–16819, http://dx.doi.org/10.1021/acs.jpcc.0c03637.
[15] K.M. Saqr, H.S. Aly, M.A. Wahid, M.M. Sies, CFD Lett. 1 (2) (2009).
[16] A. Bazgir, N. Nabhani, S. Eiamsa-ard, Appl. Therm. Eng. 144 (2018) 181–208, http://dx.doi.org/10.1016/j.applthermaleng.2018.08.043.
[17] Y. Xue, M. Arjomandi, R. Kelso, Int. J. Refrig. 36 (6) (2013) 1730–1740, http://dx.doi.org/10.1016/j.ijrefrig.2013.04.016.
[18] N. den Harder, et al., Plasma Process. Polym. 14 (2017) 1600120, http://dx.doi.org/10.1002/ppap.201600120.
[19] Alex van de Steeg, et al., ACS Energy Lett. 6 (2021) 2876–2881, http://dx.doi.org/10.1021/acsenergylett.1c01206.
[20] Lee N. Jones, Modelling of Turbulent Swirling Flows (Ph.D. thesis), The University of Leeds, 2004.
[21] M. Safavi, E. Amani, J. Turbul. 19 (1112) (2019) 10171050, http://dx.doi.org/10.1080/14685248.2018.1527033.
[22] I. Matveev, Serhiy Serbin, 44th AIAA Aerospace Sciences Meeting and Exhibit, Reno, Nevada, AIAA 2006-551, 2006, pp. 1–12, http://dx.doi.org/10.2514/6.2006-551.
[23] A. Gupta, R. Kumar, Int. J. Heat Fluid Flow 28 (2007) 249261, http://dx.doi.org/10.1016/j.ijheatfluidflow.2006.04.005.
[24] F. Chang, V.K. Dhir, Int. J. Heat Fluid Flow 15 (5) (1994) 346–356, http://dx.doi.org/10.1016/0142-727X(94)90048-5.
[25] P.M.J. Koelman, Chemical Aspects of CO_2 Plasma Modelling (Ph.D. thesis), Eindhoven University of Technology, 2019.
[26] Tafizur Rehman, Studies on Plasma-Chemical Reduction (Ph.D. thesis), Eindhoven University of Technology, 2018.
[27] J.A. van Oijen, L.P.H. de Goeij, Combust. Sci. Tech. 161 (2000) 113–137, http://dx.doi.org/10.1080/00102200008935814.
[28] A.W. van de Steeg, et al., J. Phys. Chem. Lett. 13 (2022) 1203–1208, http://dx.doi.org/10.1021/acs.jpclett.1c03731.
[29] P. Viegas, et al., Plasma Sources Sci. Technol. 29 (2020) 105014, http://dx.doi.org/10.1088/1361-6595/abb41c.
[30] David C. Wilcox, Turbulence Modeling for CFD, DCW Industries Inc, 1994, Second Printing.
[31] A.J. Wolf, T.W.H. Righart, F.J.J. Peeters, W.A. Bongers, M.C.M. van de Sanden, Plasma Sources Sci. Technol. 29 (2020) 025005, http://dx.doi.org/10.1088/1361-6595/ab5eca.
[32] A.W. van de Steeg, L. Vialetto, A.F. Silva, F.J.J. Peeters, D.C.M. van den Bekerom, N. Gatti, P. Diomede, M.C.M. van de Sanden, G.J. van Rooij, Opt. Lett. OSA 46 (2021) 2172–2175, http://dx.doi.org/10.1364/OL.42410204/2021, 04/2021.
[33] J. van Dijk, K.S.C. Peerenboom, M. Jimenez-Diaz, D.B. Mihailova, J.J.A.M. van der Mullen, The plasma modelling toolkit, J. Phys. D: Appl. Phys. 42 (19) (2009) 1940121, http://dx.doi.org/10.1088/0022-3727/42/19/194012/14.
[34] ANSYS® Fluent™ 2019 R1, 2020 R2 and its documentation.
[35] J.F.J. Janssen, Equilibrium and Transport in Molecular Plasmas (Ph.D. thesis), Eindhoven University of Technology, 2016.
[36] James N. Butler, Richard S. Brokaw, J. Chem. Phys. 26 (6) (1957) http://dx.doi.org/10.1063/1.1743596.
[37] H.K. Versteeg, W. Malalasekera, An Introduction to Computational Fluid Dynamics, second ed., Pearson Education Limited, 2007.
[38] E.V. Kustova, E.A. Nagnibeda, Chem. Phys. 321 (2006) 293–310, http://dx.doi.org/10.1016/j.chemphys.2005.08.026.
[39] M. Baghdad, A. Ouadha, O. Imine, Y. Addad, Int. J. Therm. Sci. 50 (2011) 2377–2385, http://dx.doi.org/10.1016/j.ijthermalsci.2011.07.011.